Progress In Electromagnetics Research B, Vol. 22, 73–102, 2010

RADIO ASTRONOMY AND SUPER-SYNTHESIS: A SURVEY

S. Joardar

Tata Institute of Fundamental Research
Giant Meterwave Radio Telescope
Narayagaon, Pune 410504, India

S. Bhattacharyya

Department of Electrical Engineering
Indian Institute of Technology
Kanpur 208016, India

A. B. Bhattacharya

Department of Physiscs
University of Kalyani
Kalyani, West Bengal 741235, India

C. R. Datta

Department of Electronics & Communication Engineering
Narula Institute of Technology
Agarpara, Kolkata 700109, India

Abstract—Radio astronomy has a wide electromagnetic spectrum. It is based on antennas, electronics, software etc., and thus highly technical. The radio data obtained from distant objects like stars, galaxies, pulsars etc. are useful for studying the Universe. Many of the radio emissions, especially from the Sun have been studied over decades for understanding the ionosphere and its effects on radio communication. Until now, this subject of radio astronomy has found its existence among those who are associated with astronomy and possessing at least some knowledge of RF engineering. A requirement of a review literature on this subject with technical details is felt by many working engineers and scientists. It is thus proposed to write a series of articles covering the subject from both engineering and

Corresponding author: S. Joardar (sjoardar@gmail.com).

scientific angles. This paper is the first of this series. It focuses on the foundation of this subject and briefly describes the super-synthesis technique. Overview of various concepts like cosmic radio signals, continuum, synchrotron emission etc., general instrumentation for radio astronomy, imaging techniques and radio interference have have been presented.

1. INTRODUCTION

Radio astronomy is a study of the Universe at radio wavelengths. It is based on the radio signals received from distant astronomical objects. This article gives a brief introduction to the subject, its discovery and early works, basic mechanisms responsible for generation of the radio spectrum by astronomical objects, concepts of receiving instruments, radio imaging techniques and problems of local radio interference.

The objects of radio emission may be grouped based on their nature, size, distance from Earth and the systems they form. Fig. 1 shows some flux densities measured on Earth due to radio emission from different astronomical objects. The human generated noise dominates over most of the signals obtained from distant astronomical objects. The unit of measurement is usually *jansky* named after the discoverer sir Karl Jansky. 1 $jansky = 10^{-26}\,\mathrm{W/m^2/Hz}$.

The atmosphere is also not fully transparent to the electromag-

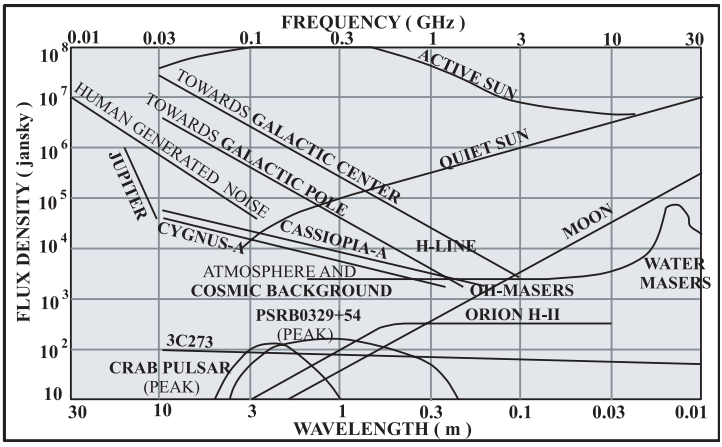

Figure 1. Flux density measured on Earth as a result of radio emission from different astronomical sources at different frequency bands.

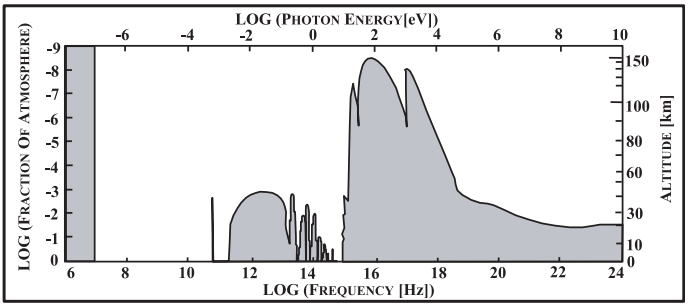

Figure 2. Transparency of the atmosphere towards electromagnetic radiations at different frequencies. The dark bounding line above the gray region indicates the height above sea level where the atmosphere becomes transparent to different frequencies [1].

netic radiations. The transparency is frequency dependent. Fig. 2 shows the transparency of atmosphere towards electromagnetic radiations at different frequencies. Thus, only limited portion of the actual radio spectrum is available on Earth.

The frequencies of interest are restricted by our atmosphere to a range of approximately 10 MHz to 300,000 MHz. Today we have a clear knowledge of different processes by which the radio waves are produced in the space. One of these is the thermal black body radiation from hot and warm objects like the Sun, the planets or cosmic background. This radiation is continuous and governed by Planck's law. Spectral line radiations result from transitions within atoms and molecules. They generally come from the clouds of gases in space and can be either due to emission or absorption. The third kind is the synchrotron radiation, emitted from charged particles moving at relativistic velocities in magnetic fields. Also, there are radiations like Bremsstrahlung caused by acceleration and deceleration of moving charged particles near the vicinity of heavier charged particles like atomic nucleus.

2. THE DISCOVERY AND EARLY-WORKS ON RADIO ASTRONOMY

Sir Karl Jansky was the first to recognize celestial nature of some radio noise at 20.5 MHz in 1932. He discovered some radio noise originating from from very distant sources [2]. Soon after he published few more papers [3–7] which showed that the Milky Way was the origin of the signal in the direction of Sagittarius.

Another radio engineer Grote Reber built his own radio telescope

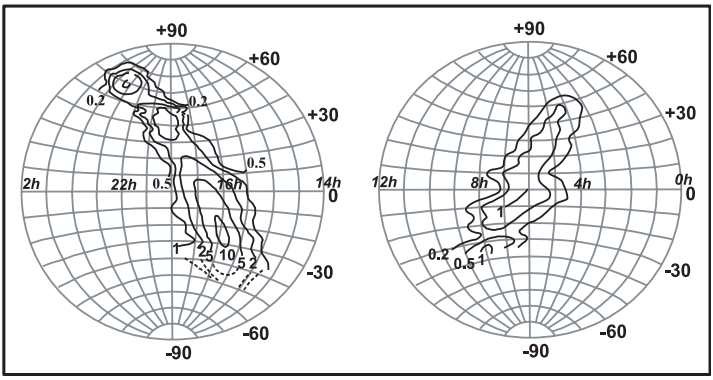

Figure 3. Reber's map of radio emission of the Galaxy at 160 MHz (1.87 m). The contours are plotted using celestial coordinates. The contours are more or less coincident with the Milky Way (Adapted from Reber, 1944 [10]).

using a paraboloid reflector having a diameter of 9.5 m. In 1939 Reber found radiation at 1.87 m and confirmed Jansky's discovery as the signal was strongest in the direction of the Milky Way [8, 9]. He further published a radio map, showing contours of equal intensity of radio noise on the celestial sphere [10]. This is shown in Fig. 3. Jan Hendrik Oort made special emphasis on Reber's paper and also suggested that there could be an emission line on radio part of the spectrum, which might be useful in the investigations of the motions of the gas from which it originated. If the amount of hydrogen in interstellar space was large enough, the 21 cm (1420 MHz) signal could be detected. Some of Reber's work are also listed in references [11, 12].

After World War II, position of some discrete radio sources were discovered using interferometry. In 1949, Australian radio astronomers were able to associate three discrete radio sources with astronomical objects. They were Crab Nebula, Centaurus A and Virgo A. Some were associated with the strange galaxies NGC 5128 and M87 [13]. In addition to the diffuse radio emission of our own Galaxy, these findings established the existence of a population of discrete radio sources, concentrated either towards the plane of the Galaxy or lying outside it. In 1951, positions of Cygnus A and Cassiopeia A were measured using an interferometer with an accuracy of about 1 arc minute. Again in 1960, another bright radio source 3C295 was found to be associated with the brightest galaxy in the cluster of galaxies [14]. Literature in the form of a book on Solar radio astronomy first appeared in 1965 [15]. Notably, a book covering technical and scientific aspects

of radio astronomy came in 1966 [16].

3. COSMIC RADIO SIGNALS: NATURE AND EMISSION

In true sense, cosmic radio signals are not as communication signals, but intensity or power radiated in the form of noise. Over a bandwidth $\Delta\nu$, where ν represents the frequency, the envelope of the radio frequency waveform has a random variation of the order of $1/\Delta\nu$. The spectral range is very large and the radiation is continuum.

3.1. Random Nature of Radio Astronomical Signals

The quiet radio emissions are random by nature. They behave as continuous random processes. The probability density function $p(x)$ of these signals could be Gaussian by nature as expressed in Eq. (1), where σ is the standard deviation (square-root of variance), μ is the mean and x is the random variable.

$$p(x) = \frac{1}{\sigma\sqrt{2\pi}} \exp\left(-\frac{(x-\mu)^2}{2\sigma^2}\right) \tag{1}$$

3.2. Basic Emission Mechanisms

Radio astronomical sources can be broadly classified as (*i*) thermal, and (*ii*) non-thermal. Thermal radiation comes from hot black body and governed by Planck's law. The non-thermal radiation may be either synchrotron radiation or Bremsstrahlung radiation.

3.2.1. Thermal Radiation

Planck's law as expressed in Eq. (2). The quantity I is known as *spectral radiance*. It is energy per unit time per unit surface area per unit solid angle per unit frequency and measured in units of $\mathrm{W\,m^2\,sr^{-1}\,Hz^{-1}}$.

$$I(\nu, T) = \frac{2h\,\nu^3}{c^2}\left(\frac{1}{e^{\frac{h\nu}{kT}} - 1}\right) \tag{2}$$

Here, ν is the radiation frequency (measured in hertz), T is the the black body temperature (in K), h is Planck's constant, c is the velocity of light and k is the Boltzmann constant. With increase in temperature the radiated energy increases rapidly and is related by Stefan-Boltzmann law as expressed in Eq. (3).

$$F = \sigma T^4 \text{ watt/m}^2 \tag{3}$$

Here, F is known as *energy flux* or power radiated per unit area from an object, and σ is the Stefan-Boltzmann constant. The luminosity is defined as the total energy radiated from an object per unit time. The surface area of a star can be estimated from its radius R as $4\pi R^2$, and thus the luminosity L of the star can be expressed as given below in Eq. (4).

$$L = 4\pi R^2 \sigma T^4 \text{ watt} \tag{4}$$

The wavelength λ_{peak} at which the emission spectra of a black body is maximum is also dependent on its temperature. It is governed by Wien's displacement law and is shown below in Eq. (5).

$$\lambda_{peak} = \frac{2.9 \times 10^{-3}}{T} \text{ m} \tag{5}$$

The observed brightness of an astronomical object from Earth, known as *apparent brightness* is the flux density that we actually receive from it per unit bandwidth $\Delta\nu$ (Hz) per unit solid angle. It is usually measured in watt $\text{m}^{-2}\,\text{Hz}^{-1}\,\text{str}^{-1}$ and is dependent on the object distance. If r is distance between the object and point of measurement, and ϕ_{obj} is the solid angular extent of the object, then the apparent brightness B may be expressed as in Eq. (6).

$$B = \frac{L}{4\pi r^2 \Delta\nu\, \phi_{obj}} \tag{6}$$

The Rayleigh-Jeans radiation law is an approximation of the Planck's law of spectral radiance at lower frequencies and is expressed in Eq. (7). It simplifies the Planck's law at the lower part of spectrum (or radio frequency band) of stars and hot regions. Fig. 4 compares

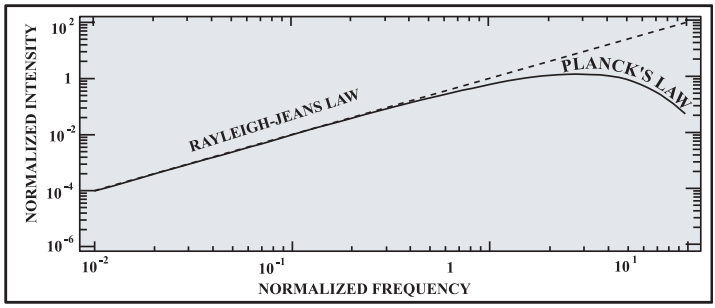

Figure 4. Comparison of Rayleigh-Jean law with Planck's law.

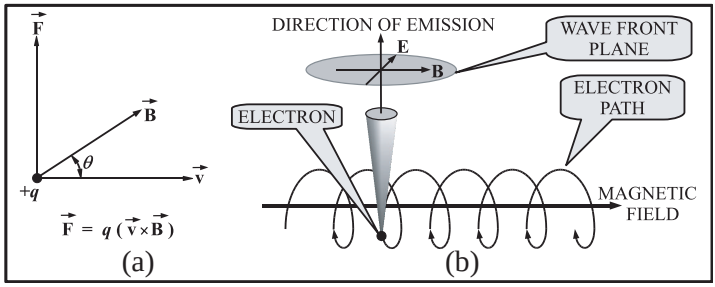

Figure 5. (a) Force on a moving charge in a magnetic field. (b) An electron at relativistic speed spirals around a magnetic field line resulting to synchrotron emission. The emission is plane polarized with its electric field tangential to the spiral path.

the Rayleigh-Jean law with the Planck's law.

$$B = \frac{2kT\nu^2}{c^2} \tag{7}$$

3.2.2. Non-thermal Radiation

Non-thermal radiations are generally (i) synchrotron radiation and or (ii) Bremsstrahlung radiation.

(i) The synchrotron radiation: This is very important, especially in Sun, Jupiter's magnetosphere, active galaxies and pulsars. The force on a moving charge in a magnetic field is equal to the cross product of the particles velocity with the magnetic field times the magnitude of the charge (Fig. 5(a)). In Fig. 5(b), an electron is trapped in a magnetic field and spins around resulting in radiation. It is concentrated along the direction of electron motion and is strongly plane polarized. Schott derived expressions for the angular distribution of the radiation as a function of the harmonic of orbital frequency [17]. Later it became well known after the works put up by Arzimovitch and Pomeranchuk [18] and Schwinger [19, 20].

The synchrotron radiation may be characterized as follows. Let the electron posses an energy E as expressed in Eq. (8), where m_e is the mass of the electron and γ is the *Lorentz Factor* as expressed in Eq. (9) with v as the velocity of the particle and c as the velocity of light. The characteristic synchrotron frequency of emission ν_c is expressed in Eq. (10), where B is the magnetic field. In actual case, the emission has a broad band spectrum, essentially from zero to the synchrotron frequency. Since high energy photons carry the bulk of

energy, we use the approximation.

$$E = \gamma\, m_e\, c^2 \tag{8}$$

$$\gamma = \frac{1}{\sqrt{1-(\frac{v}{c})^2}} \tag{9}$$

$$\nu_c = \frac{3\gamma^2 eB}{4\pi m_e c} \approx 4.2 \times 10^6 \gamma^2 B \text{ Hz} \tag{10}$$

The electrons spin around the magnetic field describing a spiral path. Let α be the pitch of the spiral of a single electron. For component of electron motion parallel to the magnetic field, we may replace the magnetic field by its perpendicular component $B \sin\alpha$, such that the pulse width Δt_p may be re-expressed as in Eq. (11).

$$\Delta t_p = \frac{1}{\gamma^2\, \omega_G\, \sin\alpha} \tag{11}$$

The power spectrum of the pulse $U(\omega)$ is proportional to square of $E_y(\omega)$ as expressed in Eq. (12), where ω_C is the critical angular frequency. A Fourier analysis of the pulse train instead of a single pulse, replaces $\sqrt{3}$ by $3/2$ thereby revealing the roll-off at frequencies less than $\omega_C/3$. Performing Fourier analysis of the radiation rate P shows the power spectrum as expressed in Eq. (13). The spectra $F(\omega/\omega_C)$ is shown in Fig. 6 [21]. For higher and lower frequencies, the spectral function $F(\omega/\omega_C)$ are respectively approximated as in Eqs. (14) and (15).

$$U(\omega) \propto E_y^2(\omega) = e^{-\omega/2\sqrt{3}\gamma^3\omega_0} \equiv e^{-\omega/\omega_C} \text{ where, } \omega_C = \sqrt{3}\gamma^3\omega_0 \tag{12}$$

$$U(\omega) = \frac{P}{\omega_C} F(\omega/\omega_C) \tag{13}$$

$$F(\omega/\omega_C) = 0.78\sqrt{x}e^{-x}, \text{ for } x \gg 1, \text{ where } x = \nu/\nu_c \tag{14}$$

$$F(\omega/\omega_C) = 1.3x^{1/3}, \text{ for } x \ll 1, \text{ where } x = \nu/\nu_c \tag{15}$$

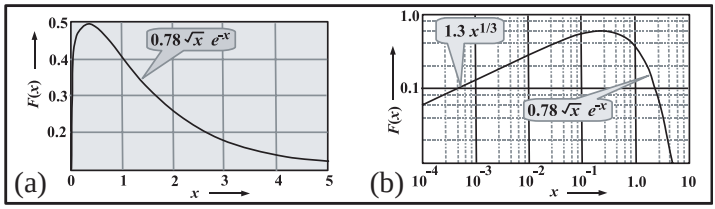

Figure 6. (a) The spectral function $F(x)$ of synchrotron radiation for $x \geq 0$. (b) Logarithmic plot of the spectral function $F(x)$ of synchrotron radiation.

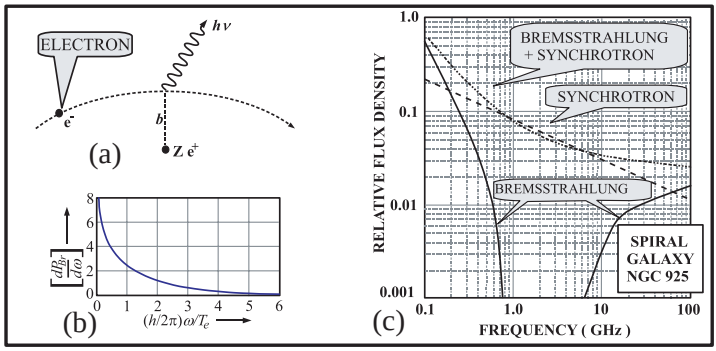

Figure 7. (a) An electron crossing an ion undergoes non-uniform acceleration/deceleration resulting Bremsstrahlung emission of photons $h\,\nu$. (b) A tentative plot of Bremsstrahlung spectrum using arbitrary units. (c) Bremsstrahlung and Synchrotron radiations from spiral galaxy NGC925 [22].

(*ii*) Bremsstrahlung radiation: It is the radiation produced by the acceleration of any charged particle when deflected by another charged particle. It has a continuous spectrum. The basic mechanism is shown in Fig. 7(a). A tentative spectrum is shown in Fig. 7(b).

It occurs in plasma from mechanical interaction of free electrons with the ions. For a uniform plasma with thermal electrons, the radiation's power spectral density is expressed as in Eq. (16), where T_e is the absolute temperature of the electrons, n_e is the number density of electrons, r_e is the classical radius of an electron, m_e is its mass, k_B is the Boltzmann constant, and c is the speed of light. The effective state of the ion charge Z_{eff} is the average over the charge states of the ions and is expressed in Eq. (17), where n_Z is the number density of ions with charge Z. The special function E_1 is defined as the exponential integral in a complex plane and is expressed in Eq. (18). The quantity w_m is expressed in Eq. (19), where k_m is a maximum or cutoff wave-number. Fig. 7(c) shows the Bremsstrahlung and Synchrotron radiations from the spiral galaxy NGC925 [22].

$$\frac{dP_{\rm Br}}{d\omega} = \frac{4\sqrt{2}}{3\sqrt{\pi}}\left[n_e r_e^3\right]^2\left[\frac{m_e c^2}{k_B T_e}\right]^{1/2}\left[\frac{m_e c^2}{r_e^3}\right] Z_{eff}\, E_1(w_m) \tag{16}$$

$$Z_{eff} = \sum_Z Z^2 \frac{n_Z}{n_e} \tag{17}$$

$$E_1(z) = \int_z^\infty \frac{e^{-t}}{t} dt, \quad |\mathrm{Arg}(z)| < \pi \tag{18}$$

$$w_m = \frac{\omega^2 m_e}{2k_m^2 k_B T_e} \tag{19}$$

4. PRINCIPLES OF RECEIVING AND DATA PROCESSING

Understanding of data processing and imaging requires a prior knowledge of engineering concepts like antenna temperature, receiver temperature, signal to noise ratio, polarization, correlations etc. as explained next.

4.1. Concept of Antenna Temperature

An isotropic antenna is placed inside a spherical cavity which acts like a perfect radiator as shown in Fig. 8(a). It behaves as a black body. The enclosed antenna receives radiations within the cavity and produces output power proportional to cavity temperature T. If the bandwidth of the antenna is $\Delta\nu$, the power output to a matched load is $kT\,\Delta\nu$, where, k is the Boltzmann constant. This appears as an electrical noise. If a practical antenna is used, the results are unchanged. In this reasoning the sky could replace the cavity (Fig. 8(b)), and the measured signal is proportional to the temperature of a portion of the sky occupied by the antenna beam. If the power at antenna terminals

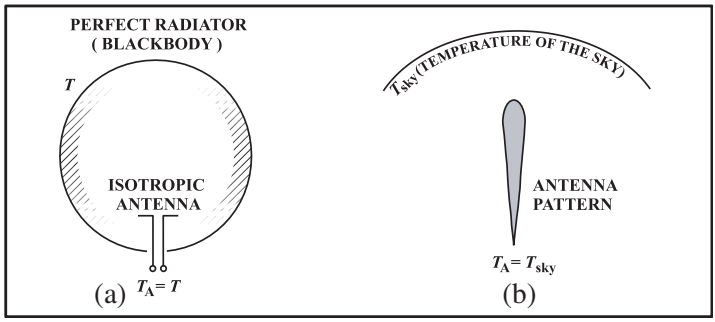

Figure 8. (a) An isotropic antenna enclosed inside a black body enclosure at a temperature T. The antenna temperature T_A is equal to the black body temperature T. (b) Sky brightness temperature T_{sky} is picked by an antenna since its pattern points towards it.

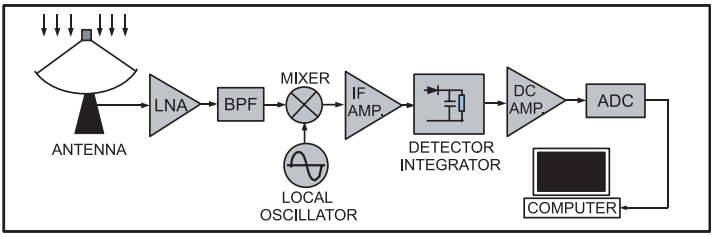

Figure 9. A basic heterodyne radio telescope receiver. The antenna, low noise RF amplifier (LNA), mixer, local oscillator, IF amplifier, detector, DC amplifier and data recording computer are shown.

(connected to a matched load) is divided by $k\,\Delta\nu$, the temperature obtained is known as *antenna temperature* T_A [16].

4.2. Concept of Source Brightness Temperature

Signals measured with radio telescope also contain noise contributed by the receiver, and from background sky (if the antenna beam is wider than the radio source). The usual practice is to make a measurement with the telescope pointed slightly away from the source in the area of the sky containing no radio sources, and next to make measurement with the telescope beam on the source. The former is subtracted from the latter giving the source contribution. The corresponding temperature is referred as *brightness temperature* T_B which is usually a function of frequency.

Measurement using an antenna depends on angular extent of the source as compared to that of the antenna beam. Three possibilities exist. (*i*) Source may have a very small angular diameter making it act as a point source. (*ii*) A discrete source has a measurable angular diameter but is smaller than the telescope's beam. (*iii*) The source size could be larger than the beam-width. For point sources, T_B provides the flux density of the radiation. In the second case, T_B is the average temperature across the source. For the third case, T_B could be different at different locations on the source itself. Thus, the antenna output will change as one scans the beam across the source [16].

4.3. Basic Radio Receiving System

A simple complete radio telescope (*radiometer*) in is shown in Fig. 9. An extremely narrow antenna beam is produced by the dish at a operating frequency ν_0. The antenna gain is assumed fixed over the observation frequency band. The signal is down converted

to intermediate frequency ν_{IF} by mixing with the local oscillator frequency ν_{LO}. An IF filter (not shown) is used before the IF amplifier. A square law detector followed by an integrator detects the signal power over a fixed integration time. It is then converted to digital using the analog to digital converter (ADC) and sent to a computer for recording. The IF conversion enables one to use different frequency antennas/antenna-feeds with the same receiver.

4.4. Improving the Signal to Noise Ratios

The continuum radio signals are extremely weak on the surface of Earth. To recover them, mathematical operations are performed at different stages of the receiver. Important of these are the correlation functions and the Wiener-Khinchin theorem.

4.4.1. Correlation Functions

Cross-correlation is a measure of similarity between two waveforms as a function of a time-lag applied to one of them. For two continuous functions of time t denoted as $f(t)$ and $g(t)$, the cross-correlation $r(\tau)$ is expressed as in Eq. (20), where f^* represents the complex conjugate of f.

$$r(\tau) = \int_{-\infty}^{\infty} f^*(\tau)\, g(t+\tau)\, d\tau \tag{20}$$

A special case of cross-correlation is the auto-correlation where the signal is correlated with itself. The auto-correlation $R(\tau)$ of a continuous functions of time t denoted as $f(t)$ is expressed in Eq. (21).

$$R(\tau) = \int_{-\infty}^{\infty} f^*(\tau)\, f(t+\tau)\, d\tau \tag{21}$$

4.4.2. Wiener-Khinchin Theorem

It says that the power spectral density of a wide sense stationary random process is the Fourier transform of the corresponding auto-correlation function. Mathematically, if $S(\nu)$ is the power spectral density of a continuous random signal $x(t)$, then it may be expressed as the Fourier transform of the auto-correlation function $R(\tau)$. It is given in Eq. (22).

$$S(\nu) = \int_{-\infty}^{\infty} R(\tau)\, e^{-j2\pi\nu\tau}\, d\tau \tag{22}$$

4.5. Radio Arrays

Array are constructed to synthesize a large aperture using several small antennas. This requirement arises from the practical limitation of constructing a large single antenna. The principles are explained here.

4.5.1. Filled Array

An aperture strip having an area A is show in Fig. 10(a). A near approximation is done using four parabolic dishes. A is approximately the sum of the individual aperture areas (Eq. (23)). This is satisfactory until the source is at zenith. All delays are kept identical (Eq. (24)). In Fig. 10(b), time delays have been introduced for phased addition of power from the same wave-fronts.

$$A \approx A_1 + A_2 + A_3 + A_4 = \sum_{i=1}^{4} A_i \tag{23}$$

$$\tau_1 = \tau_2 = \tau_3 = \tau_4 \tag{24}$$

In Fig. 10(c), if the source is inclined at an angle from the zenith, the wave-fronts (WF) approaching the antennas are different. The separation between any antenna pair is d. Artificial delays are adjusted

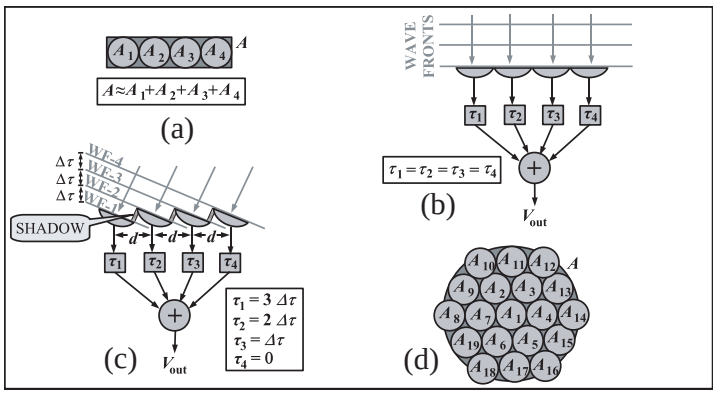

Figure 10. (a) A rectangular aperture is synthesized using four circular apertures. (b) Four dish antenna pointed to zenith. The same wavefront reaches all the individual antenna apertures. (c) Four antennas are tracking a radio source away from the zenith. Since different wave-fronts reach different antennas, time delays are introduced for phased summation. (d) Synthesis of a large circular aperture using small circular apertures.

before combining the signals (Eq. (25)). When dish are inclined, shadows are cast by adjacent antennas and effective aperture area reduces. Fig. 10(d) shows a large circular aperture synthesized using small circular apertures. This type of arrays are seldom used.

$$\left.\begin{aligned}\tau_1 &= 3\,\Delta\tau\\ \tau_2 &= 2\,\Delta\tau\\ \tau_3 &= \Delta\tau\\ \tau_4 &= 0\end{aligned}\right\} \tag{25}$$

4.5.2. Phased Grating Array

These are used for pulsar observations. A one dimensional phased array is shown in Fig. 11(a). The source inclination angle is θ. The antennas are separated by a distance d from each other. No shadows are cast since d is much larger than individual antenna diameters. Any wave-front first reaches the right-most antenna. It reaches the next antenna after a time delay $\Delta\tau = d\sin\theta/c$ and so on, where c is the velocity of wave propagation. Fig. 11(b) shows the normalized power patterns of (*i*) a single dish, and (*ii*) an array of isotropic antennas. The array response resembles a grating. The angular distance between two adjacent crests is known as *grating interval*. It depends on the d, size of the dishes and the wavelength λ. The effective pattern is shown

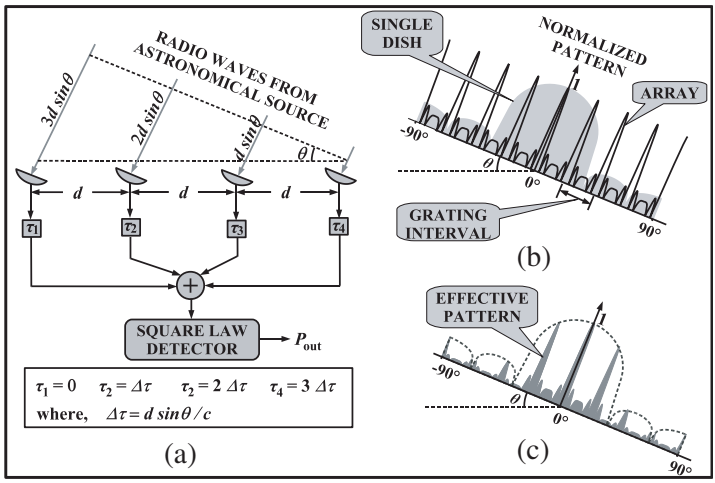

Figure 11. A grating array and its response. (a) Signals are added after phase correction using appropriate delays. (b) Normalized power patterns of a dish and an array of isotropic antennas. (c) Effective system response.

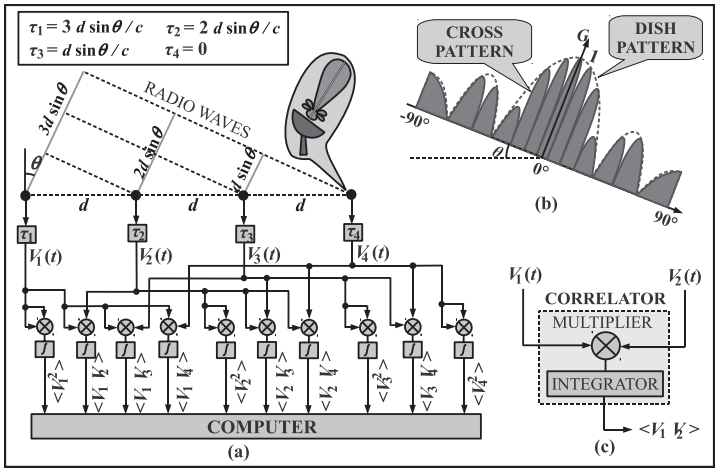

Figure 12. A correlator array using four antennas. (a) The signals from each antenna pair are correlated and saved in a computer. (b) A tentative plot of the fringe pattern formed from cross-correlations. (c) A basic correlator unit.

in Fig. 11(c). The grating side lobes appear modulated by the single dish response. The phased array output P_{out} is of the form expressed in Eq. (26), where the number of antennas is n_a. The number of cross products n_c is given as in Eq. (27). The number of self products is equal to the number of antennas n_a.

$$P_{out} = (V_1 + V_2 + V_3 + \ldots)^2 = \left(\sum_{i=1}^{n_a} V_i \right)^2 \tag{26}$$

$$n_c = n_a (n_a - 1) \tag{27}$$

If the paths from each antenna to the detector posses identical electrical length, the signals combine in phase provided the incoming radiation is inclined at an angle θ given by Eq. (28). Here, N is an integer, λ is the wavelength, and d is distance of separation between adjacent antennas.

$$\theta = \sin^{-1} \left(\frac{N\lambda}{d} \right), \quad N = 0, 1, 2 \ldots \tag{28}$$

4.5.3. Correlator Arrays

Correlator arrays are used for higher angular resolution. Fig. 12(a) shows a correlator array using four dish antennas. The auto and cross correlation results are saved by a computer. Like phased arrays,

artificial delays are employed. These are expressed in Eq. (29), where d is the separation between the antennas. Fig. 12(b) shows a tentative plot of the radiation pattern formed by an antenna pair cross-correlation product. The beam splits forming a fringe like pattern. The number of lobes increases if either d is increased or the wavelength is reduced. Fig. 12(c) shows a basic correlator unit consisting of a multiplier followed by an integrator. Integration in time improves the signal to noise ratio. The output contain $r(\tau)$ and $R(\tau)$ defined by Eqs. (20) and (21).

If $V_1(t) = v_1 \cos(2\pi\nu t)$ and $V_2(t) = v_2 \cos(2\pi\nu(t - \tau_g))$ are the output voltages from any two antennas, which are fed to the correlator unit shown in Fig. 12(c), the correlator output $r(\tau_g)$ can be expressed in Eq. (30). Here τ_g is the relative delay between the two input signals, and ν is the frequency. For n_a number of antennas, the number of cross correlations is n_{cc} and auto correlations is n_{ac} as expressed in Eqs. (31) and (32). These values are saved along with time, frequency, bandwidth and the antenna coordinates (u, v, w). These are essential requirements for constructing the radio images.

$$\left.\begin{aligned} \tau_1 &= 3\,\Delta\tau = 3d\sin\theta \\ \tau_2 &= 2\,\Delta\tau = 2d\sin\theta \\ \tau_3 &= \Delta\tau = d\sin\theta \\ \tau_4 &= 0 \end{aligned}\right\} \tag{29}$$

$$r(\tau_g) = v_1\, v_2\, \cos 2\pi\nu(\tau_g) \tag{30}$$

$$n_{cc} = n_a(n_a - 1)/2 \tag{31}$$

$$n_{ac} = n_a \tag{32}$$

One of the largest meter-wave correlator arrays called the *Giant Meter-wave Radio Telescope* (GMRT) is located near Narayangaon (80 km North of Pune), India. An aerial picture is shown in Fig. 13. It uses 30 steerable antennas each having a diameter of 45 meters spread in Y-configuration. The operating center frequencies range roughly from 120 MHz to 1500 MHz with a bandwidth of 32 MHz.

5. CONSTRUCTING THE RADIO IMAGES

Radio intensity-images of the observed sources are prepared from the data obtained from radio telescopes. Usually interferometer radio array is preferred.

5.1. The Basic Mapping Technique

Figure 14(a) shows a highly directional single dish radio telescope pointed towards a distant radio astronomical source. Parallel rays

Figure 13. Aerial photograph of some antennas of the GMRT located about 80 km North of Pune (India). Courtesy: Google Map.

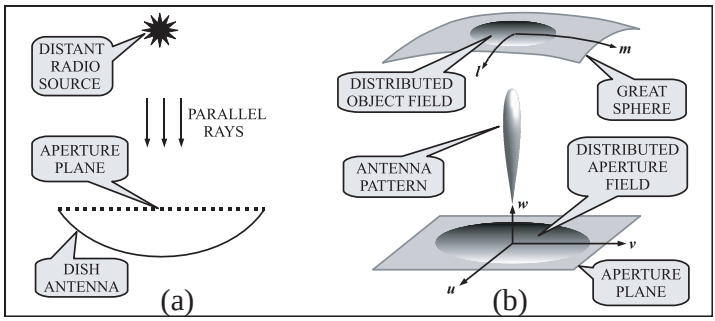

Figure 14. (a) A distant radio astronomical source illuminates a dish antenna with parallel rays. (b) Electric field distributions of the source (on the great sphere) and antenna aperture (on the aperture plane) are tentatively illustrated.

illuminate the dish aperture. Let the aperture plane be placed at the origin of a rectangular coordinate system (u, v, w) with w pointing towards the source (Fig. 14(b)). On the sky, let the two dimensional electric field distribution be centered on another coordinate system (l, m). On the u-v plane, the electric field distribution $\mathcal{E}(u, v)$ is a result of the electric field distribution $V(l, m)$ on the sky. Assuming that we know the function $\mathcal{E}(u, v)$ completely, we take the auto-correlation of each of the electric field points on the u-v plane and represent them as $W(u, v)$. Applying a Fourier transform on $W(u, v)$, the intensity field distribution $I(l, m)$ of the source is obtained. Though practically it is not possible to know the function $\mathcal{E}(u, v)$ since the antenna produces

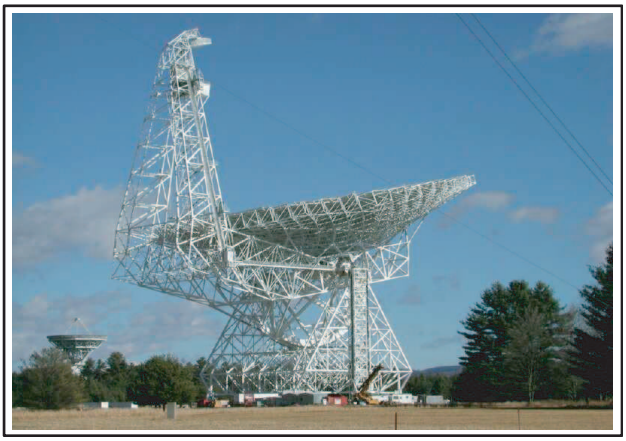

Figure 15. GBT is the world's largest steerable single dish radio telescope located at NRAO, West Virginia.

a single output, this result is still very important as it establishes a basic relation between intensity map of radio source on the sky with the aperture illumination.

Construction of single dish radio telescopes are limited by their physical size. Fig. 15 shows the world's largest steerable single dish radio telescope named as the *Green Bank Telescope* (GBT) located at NRAO, West Virginia. Single dish radio telescopes can be advantageous in making preliminary surveys of the sky at low resolution. Moreover, its data can be combined with interferometer to obtain a good balance between lower and higher spatial frequency components. Fig. 16 shows a radio image of the Cygnus-X region at a frequency of 790 MHz. The beam-width of the GBT at this frequency is approximately 16 arc minutes. This observation was made by the GBT commissioning team led by Ron Maddalena.

5.2. The Basic Super-synthesis Technique

Instead of a single antenna, an antenna array aided with the rotation of Earth can synthesize a large antenna aperture. This technique was named by Martin Ryle as *super-synthesis* [24–27].

Consider a large number of antennas spread over a plane area at some latitude between 20° and 70° (Fig. 17(a)). They track a distant radio source located on the celestial North pole. Consider a rectangular coordinate system (u', v', w') whose origin in located near the center of the antenna plane (Fig. 17(b)). The w' axis points towards the celestial

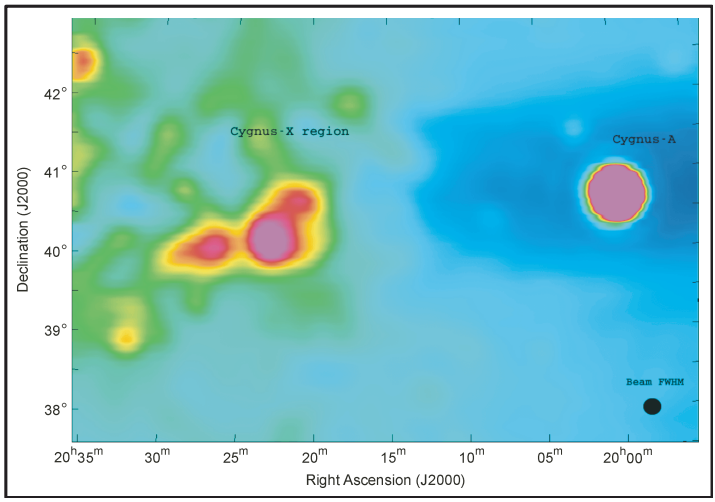

Figure 16. An image of the Cygnus-X region at 790 MHz, made during the commissioning of GBT. The signals from Cygnus-A is completely saturated. Copyright NRAO/AUI/NSF.

North pole (source). The u'-v' plane is kept stationary to the source. As seen from the source towards the antennas, due to the rotation of the Earth, the position of the antennas will appear to be moving over u'-v' plane. The loci a', b' and c' respectively of the antennas a, b and c on the u'-v' plane will be circles over a period of 24 h. At very short intervals of time, one may record the outputs of individual antennas and place them on the u'-v' plane. If there are many antennas at different radial distances from the origin of the u', v', w' coordinates, then over a period of 24 h the u'-v' plane gets highly populated. The u'-v' plane forms the aperture of a large synthesized antenna. Thus after proper calibration of the data one may apply Fourier transform on the u-v plane data to obtain the the field distribution of the source.

For a radio source on the celestial equator (Fig. 17(c)), the loci a', b' and c' on the u-v plane are straight lines. Thus if all the antennas are posited on a single East-West line then all the loci will fall on a single straight line, which is not sufficient for making a radio image. It is necessary to have some antennas separated along the North-South axis.

If the radio source under observation is located at a celestial latitude greater than $0°$ and less than $90°$ or greater than $-90°$ and less than $0°$, each of the loci will be an ellipse. This is shown in Fig. 17(d).

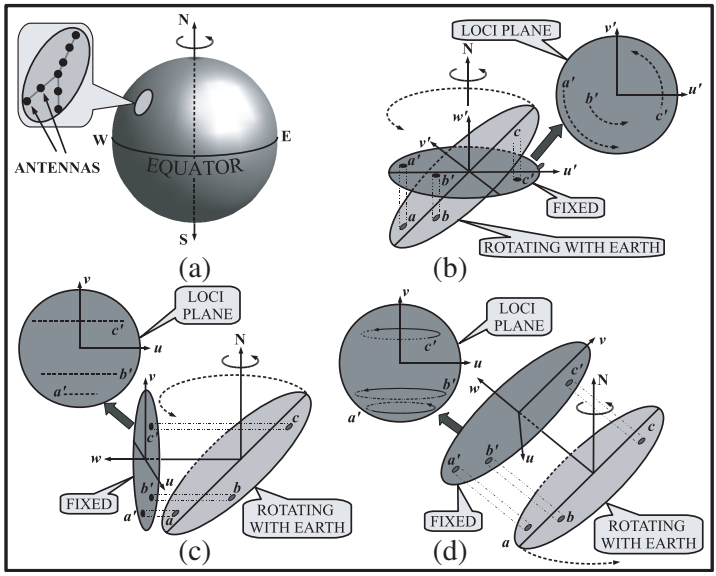

Figure 17. Principle of super synthesis. (a) An array of antennas rotates with the Earth rotation. (b) Observing a radio source towards celestial North Pole. (c) Observing a radio source along the celestial equator. (d) Observing a radio source along a celestial latitude in between.

5.3. Super-synthesis Using Correlator Arrays

The correlation products between any pair of antennas are used to fill the u-v plane. The (u, v, w) coordinates has dimensions in number of wavelengths. As shown in Eq. (31), if there are n_{cc} antennas in the array, the number of cross correlation terms is $n_{cc}(n_{cc}-1)/2$. Thus the u-v plane gets populated very well. In a two antenna interferometer, if we fix one of the antennas at the origin of the (u, v, w), then a line joining the two antennas on the u-v plane will rotate through 180° in 12 h. Similar observation results if the other antenna is considered as the origin of the (u, v, w) coordinates. Thus, in principle it is possible to cover 360° of baseline rotation in only 12 h.

The output from an interferometer is a measure of the spatial coherence function called *visibility* and is represented by $\mathcal{V}(u, v)$. The visibility values obtained from a 12 h observation covers only one half of the u-v plane. But one can derive the values of visibilities on the other half using Eq. (33), where $\mathcal{V}^*(u, v)$ is the complex conjugate of $\mathcal{V}(u, v)$. Thus, from a 12 h observation, one derives 24 h of observed

data.

$$\mathcal{V}(-u,-v) = \mathcal{V}^*(u,v) \tag{33}$$

5.3.1. Relation between Visibility and Correlation

A radio image visibility is computed from the cross correlations $r(\tau_g)$ on the u-v plane and then apply a Fourier transform. The visibility are actually scaled cross correlations. Strictly speaking, it is a function of the u, v, w coordinates and is represented as $\mathcal{V}(u, v, w)$. These are explained next.

Consider a two element interferometer observing a radio source (Fig. 18(a)). Let antenna-1 be posited at the origin of a u, v, w coordinate system. Let $I(l, m)$ be the intensity distribution of the source on the celestial sphere. The signal phases obtained from any point on the radio source is measured with respect to a reference point on the source known as the *phase reference position*. Let the origin of the l, m coordinate system be at the phase reference position. Let $I(\bar{s})$ be the intensity/brightness of the sky at a frequency ν in the direction $\bar{s}$. Let $A(\bar{s})$ be the effective aperture area of an antenna in the same direction. Then the signal power received over a bandwidth $\Delta\nu$ within a solid angular element $d\Omega$ by each antenna is $A(\bar{s})\, I(\bar{s})\, \Delta\nu\, d\Omega$. The correlated signal power dr over $d\Omega$ is expressed in Eq. (34).

$$dr = A(\bar{s})\, I(\bar{s}) \Delta\nu\, d\Omega \cos(2\pi\nu\tau_g) \tag{34}$$

Integrating Eq. (34) over the celestial sphere we obtain the correlator

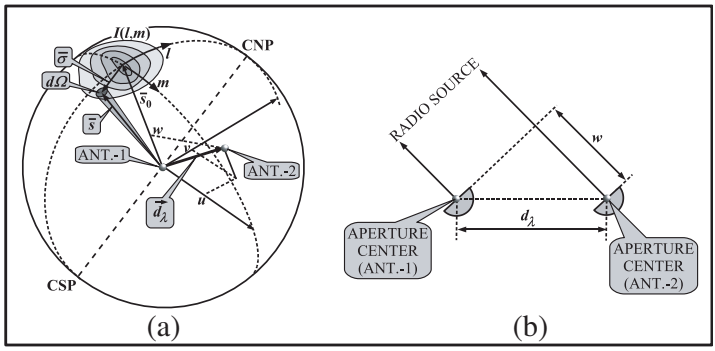

Figure 18. Geometry of the radio source and the antennas. (a) A radio source with intensity distribution $I(l, m)$ is being observed using a simple two element radio interferometer. (b) Lower the elevation angle of the radio source the larger the value of w.

power r as in Eq. (35), where $\vec{d_\lambda}$ is the baseline vector.

$$r(\vec{d_\lambda}, \bar{s}) = \Delta\nu \int A(\bar{s})\, I(\bar{s})\, \cos\left[2\pi\left(\vec{d_\lambda} \cdot \bar{s}\right)\right] d\Omega \tag{35}$$

We make measurements with respect to the phase reference position $\bar{s_0}$. We may thus express $\bar{s} = \bar{\sigma} + \bar{s_0}$, where $\bar{\sigma}$ is the space vector from the phase reference point to the observing point. Re-expressing r we get Eq. (36). It is assumed that the source is spatially incoherent.

$$\begin{aligned} r\left(\vec{d_\lambda}, \bar{s_0}\right) = \Delta\nu\, \cos\left[2\pi\left(\vec{d_\lambda} \cdot \bar{s_0}\right)\right] \int A\left(\bar{\sigma}\right)\, I\left(\bar{\sigma}\right)\, \cos\left[2\pi\left(\vec{d_\lambda} \cdot \bar{\sigma}\right)\right] d\Omega \\ -\Delta\nu \sin\left[2\pi\left(\vec{d_\lambda} \cdot \bar{s_0}\right)\right] \int A(\bar{\sigma}) I(\bar{\sigma}) \sin\left[2\pi\left(\vec{d_\lambda} \cdot \bar{\sigma}\right)\right] d\Omega \end{aligned} \tag{36}$$

The visibility $\mathcal{V}$ is a complex function and can be defined as in Eq. (37), where $A'(\bar{\sigma}) \equiv A(\bar{\sigma})/A_0$ is the normalized antenna beam pattern. Note that A_0 is the peak antenna gain (along the source direction). Separating real and imaginary parts we obtain Eqs. (38) and (39).

$$\mathcal{V} = |\mathcal{V}|\, e^{j\phi_v} = \int A'\left(\bar{\sigma}\right) I\left(\bar{\sigma}\right)\, e^{-j2\pi\vec{d_\lambda}\cdot\bar{\sigma}}\, d\Omega \tag{37}$$

$$|\mathcal{V}| \cos\phi_v = \int A'\left(\bar{\sigma}\right) I\left(\bar{\sigma}\right)\, \cos\left(2\pi\vec{d_\lambda} \cdot \bar{\sigma}\right) d\Omega \tag{38}$$

$$|\mathcal{V}| \sin\phi_v = -\int A'\left(\bar{\sigma}\right) I\left(\bar{\sigma}\right) \sin\left(2\pi\vec{d_\lambda} \cdot \bar{\sigma}\right) d\Omega \tag{39}$$

Relating the above with Eq. (36) we obtain Eq. (40) as shown below.

$$r\left(\vec{d_\lambda}, \bar{s_0}\right) = A_0\, \Delta\nu\, |\mathcal{V}| \cos\left[2\pi\left(\vec{d_\lambda} \cdot \bar{s_0} - \phi_v\right)\right] \tag{40}$$

The above equation explains that an interferometer is an instrument for measuring the visibility which is the spacial coherence function with a different normalization.

5.3.2. The Van Cittert-Zernike Equation

To create a radio image, one has to make use of the Eq. (40) and find their positions on the u, v, w coordinate system and relate them with l, m coordinate system. In an interferometer, w increases as the elevation angle of the source reduces (Fig. 18(b)) as shown in Eq. (41).

$$\vec{d_\lambda} \cdot \bar{s} = ul + vm + wn \tag{41}$$

When $\bar{s} = \bar{s}_0$, Eq. (41) simplifies to Eq. (42). We may define an infinitesimal solid angle $d\Omega$ as expressed in Eq. (43) and expand it by

substituting $n = \sqrt{1 - l^2 - m^2}$.

$$\vec{d_\lambda} \cdot \bar{s_0} = w \tag{42}$$

$$d\Omega = \frac{dl\,dm}{n} = \frac{dl\,dm}{\sqrt{1 - l^2 - m^2}} \tag{43}$$

We may now express the visibility $\mathcal{V}$ from Eq. (40) as a function of u, v, w as shown below in Eq. (44).

$$\mathcal{V}(u,v,w) = \iint \frac{A'(l,m)I(l,m)}{\sqrt{1-l^2-m^2}} e^{-j2\pi\left[ul+vm+w\left(\sqrt{1-l^2-m^2}-1\right)\right]} dl dm \tag{44}$$

Eq. (44) is known as *van Cittert-Zernike equation* [23, 27–30] which indicates that the visibility, $\mathcal{V}(u, v, w)$, is a Fourier-like integral of sky brightness, $I(l, m)$, multiplied by the primary beam response, $A(l, m)$, and $1/\sqrt{1 - l^2 - m^2}$. If the source extent is small, $|l|$ and $|m|$ are sufficiently small so that the term $w(\sqrt{1 - l^2 - m^2} - 1)$ in the exponent can be neglected. Thus one obtains Eq. (45). We may write the inverse transform as in Eq. (46).

$$\mathcal{V}(u,v,w) \simeq \mathcal{V}(u,v,0) = \iint \frac{A'(l,m)I(l,m)}{\sqrt{1-l^2-m^2}}\, e^{-j2\pi(ul+vm)} dl dm \tag{45}$$

$$\frac{A'(l,m)\,I(l,m)}{\sqrt{1-l^2-m^2}} = \iint \mathcal{V}(u,v) e^{j2\pi(ul+vm)} du dv \tag{46}$$

5.3.3. Filling the u-v Plane with Visibilities

Let the phase reference position of radio source under observation be (H_0, δ_0) in local equatorial coordinate system. If X_λ, Y_λ and Z_λ are

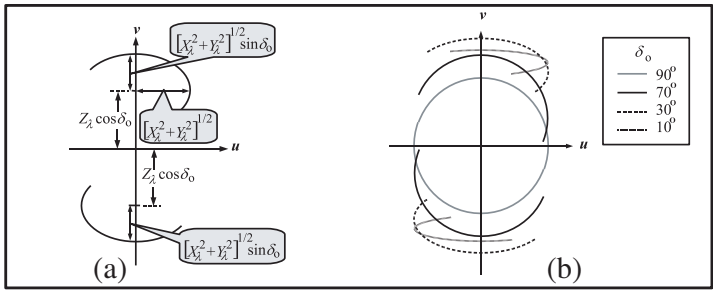

Figure 19. Locus of Eq. (47) on the u, v plane. (a) Locus of the ellipse on u, v plane for a baseline with non-zero Z_λ observing a radio source at declination δ_0. (b) Cases for different declinations.

components of baseline in a rectangular coordinate system (scaled with number of wavelengths) [23], one may express u and v as in Eq. (47).

$$u^2 + \left(\frac{v - Z_\lambda \cos \delta_0}{\sin \delta_0} \right)^2 = X_\lambda^2 + Y_\lambda^2 \tag{47}$$

Eq. (47) represents an ellipse which splits into two in the u, v plane if Z_λ is not zero [23]. Fig. 19(a) shows this while observing a radio source at declination δ_0. The length of the minor axis (along v) reduces with

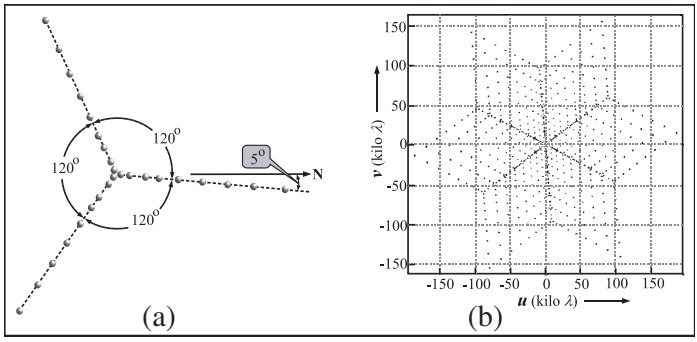

Figure 20. Filling the u-v plane with visibilities. (a) The VLA consists of 27 antennas in Y-configuration. (b) The u-v plane coverage at any instant of time obtained from a source at the zenith.

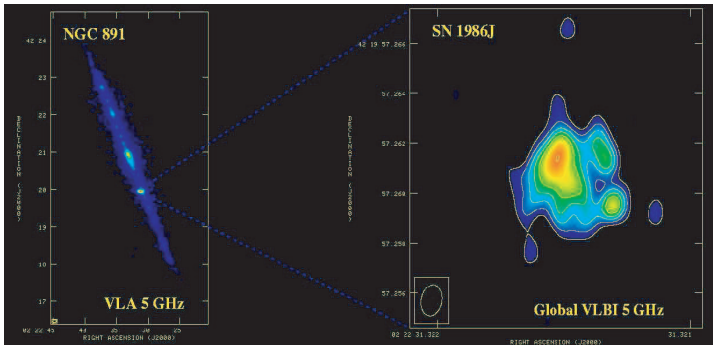

Figure 21. A radio picture of a supernova SN 1986J within the galaxy NGC 891 taken at 5 GHz. The left panel shows the galaxy NGC 891 using the VLA. The brightest red spot is the supernova SN 1986J. In the right panel the details of the supernova are shown which was made using VLBI. The investigators are M. A. Perez-Torres, A. Alberdi, J. M. Marcaide, J. C. Guirado, L. Lara, F. Mantovani, E. Ros., and K. W. Weiler. Copyright NRAO/AUI/NSF.

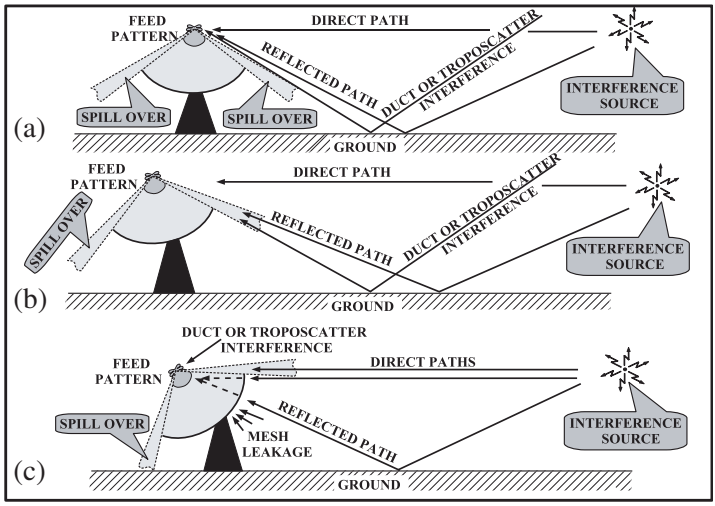

Figure 22. RFI through antenna in VHF/UHF bands. (a) RFI through side-lobes when antenna points to zenith. (b) RFI through spill-over and side lobes when antenna makes a small angle with zenith. (c) RFI through spill-over, mesh leakage and side lobes when antenna makes a large angle with zenith.

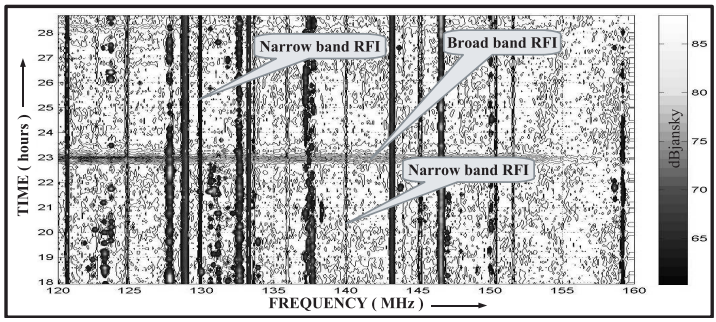

Figure 23. Examples of narrow and broad band RFI. The flux density available near an antenna is plotted in gray levels as functions of time and frequency. The unit $dbjansky = 10\log_{10}(jansky)$.

δ_0. Fig. 19(b) shows cases of a North-South baseline for different values of δ_0. The VLA (very large array, New Mexico) consists of twenty seven observing antennas posited in Y-configuration as shown in Fig. 20(a). Fig. 20(b) shows the u-v plane coverage at any instant of time with radio source is towards the zenith. The star-like structure rotates along

with Earth. If the zenith coincides with a celestial pole, then each point traces out a circle. Otherwise, the tracings could be elliptical, broken ellipse, or straight line (zero declination). With increasing time, more data fill the u-v plane. Position of the antennas are adjusted so that each baseline is unique. If the u-v plane coverage is not sufficient for a 12 h observation, VLA baselines can be re-adjusted for additional data. Using Eq. (46) the intensity distribution $I(l, m)$ or radio image of the source is made (after data calibration) [23, 27–30]. For FFT operation, the scattered data on u-v plane is interpolated on a uniform grid [23, 31, 32]. Simultaneously, the synthesized beam is controlled by a process called tapering [23]. It minimizes the side lobes of the synthesized antenna beam. After FFT the image obtained is called the *dirty image*, for it may contain many artifacts. These are removed using CLEAN [33–36] or MEM algorithms [37–39]. Fig. 21 shows a radio picture of a supernova.

6. RADIO INTERFERENCES

The signals of radio astronomy are extremely weak with respect to the man made radio signals noise. A locally generated radio noise may obscure the astronomical signal. A noise or a signal of any kind interfering with the astronomical signals is termed as radio frequency interference (RFI) [40–43].

The RFI occurs in radio data through (*i*) side-lobes of the telescope-antenna, (*ii*) mesh leakage, (*iii*) spill overs and (*iv*) leakage through the shielding of cables and electronic receiver system. Fig. 22 shows three of the possible ways of RFI in a VHF/UHF radio telescope. RFI can be broadly categorized into two [41–43]: (*i*) narrow band RFI, and (*ii*) broad band RFI. The former is usually produced from communication transmitters. The latter can be from arc wielding, ignition in motor vehicles etc. An example of narrow and broad band RFI is shown in Fig. 23. Several RFI mitigation techniques are applied before the radio image is prepared from visibilities [44].

Further information on radio astronomy may be obtained from references [45, 46].

7. CONCLUSION

Today, many of these techniques are applied in different fields of engineering. Synthetic aperture radiometer is used in solar wind remote sensing [47]. Extensive use of synthetic aperture and image processing techniques are used in RADARS [48–51]. Radiometers are

used in near field imaging using artificial satellites [52]. Space borne radiometers shows a promising monitoring of soil moisture [53].

At a first glance, it seems that radio astronomy has added a spectral window to astronomy. A closer look reveals that it has played a greater role in antenna technology, remote sensing, EM spectrum, RF and digital electronics, RFI, imaging and synthesis, etc. throughout the last eighty years. It further promises great outcomes in technology and science. In later articles, it is proposed to describe many of these and related materials more elaborately.

ACKNOWLEDGMENT

The authors are thankful to *The Electromagnetic Academy* and *PIER* and the unknown reviewers of this article.

REFERENCES

1. Giacconi, R., H. Gursky, and L. P. van Speybroeck, "Observational techniques in X-ray astronomy," *Ann. Rev. Astro. & Astroph.*, Vol. 6, 373–416, 1968.
2. Jansky, K. G., "Directional studies of atmospherics at high frequencies," *Proc. IRE*, Vol. 20, No. 12, 1920–1932, 1932.
3. Jansky, K. G., "Electrical disturbances apparently of extraterrestrial origin," *Proc. IRE*, Vol. 21, 1387–1398, 1933.
4. Jansky, K. G., "Radio waves from outside the solar system," *Nature*, Vol. 132, 66–66, 1933.
5. Jansky, K. G., "Electrical phenomena that apparently are of interstellar origin," *Popular Astronomy*, Vol. 41, 548, Dec. 1933.
6. Jansky, K. G., "A note on the source of interstellar interference," *Proc. IRE*, Vol. 23, 1158–1163, 1935.
7. Jansky, K. G., "Minimum noise levels obtained on short-wave radio receiving systems," *Proc. IRE*, Vol. 25, 1517–1530, 1937.
8. Reber, G., "Cosmic Static," *Proc. IRE*, Vol. 28, 68–70, 1940.
9. Reber, G., "Cosmic Static," *Proc. IRE*, Vol. 30, 367–378, 1942.
10. Reber, G., "Cosmic Static," *Astroph. J.*, Vol. 100, 279–287, 1944.
11. Reber, G., "Early radio astronomy at wheaton, illinoiss," *Proc. IRE*, Vol. 46, 15–23, 1958.
12. Reber, G., "A play entitled the beginning of radio astronomy," *J. Royal Astro. Soc. Canada*, Vol. 82, No. 3, 93–106, 1988.
13. Bolton, J. G., G. J. Stanley, and O. B. Slee, "Positions of three

discrete sources of galactic radio-frequency radiation," *Nature*, Vol. 164, 101–102, 1949.

14. Minkowski, R., "A new distant cluster of galaxies," *Astroph. J.*, Vol. 132, 908–910, 1960.
15. Kundu, M. R., *Solar Radio Astronomy*, Interscience Pub., New York, 1965.
16. Kraus, J. D., *Radio Astronomy*, McGraw-Hill, Inc. 1966.
17. Schott, G. A., *Electromagnetic Radiation*, Cam. Univ. Press, 1912.
18. Arzimovitch, L. and I. Pomeranchuk, "The radiation of fast electrons in the magnetic field," *J. Phy.*, Vol. 9, 267–276, 1945.
19. Schwinger, J., "On the classical radiation of accelerated electrons," *Phy. Rev.*, Vol. 75, No. 12, 1912–1925, 1949.
20. Schwinger, J., "The quantum correction in the radiation by energetic accelerated electrons," *Proc. Nat. A. S.*, Vol. 40, 132–136, 1954.
21. Ichimaru, S., *Basic Principles of Plasmas Physics: A Statistical Approach*, W. A. Benjamin, Inc., New York, 1973.
22. Duric, N., E. Bourneuf, and P. C. Gregory, "The separation of synchrotron and bremsstrahlung radio emissions in spiral galaxies," *Astro. J.*, Vol. 96, 81–91, 1988.
23. Thompson, A. R., J. M. Moran, and G. W. Swenson, Jr., *Interferometry and Synthesis in Radio Astronomy*, 2nd edition, John Wiley & Sons Inc., 2001.
24. Machin, K. E., M. Ryle, and D. D. Vonberg, "The design of an equipment for measuring small radio frequency noise powers," *Proc. IEEE*, Vol. 99, 127–134, 1952.
25. Ryle, M., "A new radio interferometer and its application to the observation of weak radio stars," *Proc. R. Soc.*, Vol. 211, 351–375, 1952.
26. Swenson, G. W. and N. C. Mathur, "The interferometer in radio astronomy," *Proc. IEEE*, Vol. 56, 2114–2130, Dec. 1968.
27. Thompson, A. R. and R. N. Bracewell, "Interpolation and fourier transformation of fringe visibilities," *Astro. J.*, Vol. 79, No. 1, 11–24, 1974.
28. Bracewell, R. N., "Inversion of non planar visibilities," *Astro. J.*, Vol. 96, No. 1, 81–91, 1984.
29. Sault, R. J. and T. A. Osterloo, "Imaging algorithm in radio astronomy," *IAU/URSI Indir. Imag.*, 177–183, Cam. Univ. P., 2007.
30. Rau, U., S. Bhatnagar, M. A. Voronkov, and T. J. Cornwell,

"Advances in calibration and imaging techniques in radio interferometry," *Proc. IEEE*, Vol. 97, 1472–1481, 2009.

31. Fu, C. and J. Wu, "Wavelet interpollation algorithm for synthetic aperture radiometer," *PIERS Online*, Vol. 1, No. 5, 510–514, 2005.
32. Zhang, C., J. Wu, and W. Sun, "Applications of Pseudo-Polar FFT in synthetic aperture radiometer imaging," *PIERS Online*, Vol. 3, No. 1, 25–30, 2007.
33. Hogbom, J. A., "Aper. synth. with non-reg. distri. of interfer. baselines," *Astro. & Astroph. Supp. Ser.*, Vol. 15, 417–426, 1974.
34. Clark, B. J., "An efficient implementation of the algorithm clean," *IEEE J. Sel. Top. on Sig. Proc.*, Vol. 89, 377, 1980.
35. Cornwell, T. J., "Multi-scale CLEAN deconvolution of radio synthesis images," *Astro. & Astroph.*, Vol. 2, 793–801, 2008.
36. Camps, A., J. Bar'a, F. Torres, and I. Corbella, "Extension of the clean technique to the microwave imaging of continuous thermal sources by means of aperture synthesis radiometers," *Progress In Electromagnetics Research*, Vol. 18, 67–83, 1998.
37. Frieden, B. R., "Restoring with maximum likelihood and maximum entropy," *J. Opt. Soc. Am.*, Vol. 62, 511–518, 1972.
38. Cornwell, T. J. and K. F. Evans, "A simple maximum entropy image deconvolution algorithm," *Astro. & Astroph.*, Vol. 143, 77–83, 1985.
39. Narayan, R. and R. Nityananda, "Maximum entropy image restoration in astronomy," *Ann. Rev. Astro. & Astroph.*, Vol. 62, 127–170, 1986.
40. Joardar, S. and A. B. Bhattacharya, "Simultaneous resolving of frequency separated narrow band terrestrial radio sources by multi antenna spectrum monitoring systems assisting radio astronomy," *Journal of Electromagnetic Waves and Applications*, Vol. 20, No. 9, 1195–1209, 2006.
41. Joardar, S. and A. B. Bhattacharya, "Algorithms for categoric analysis of of interference in low frequency radio astronomy," *Journal of Electromagnetic Waves and Applications*, Vol. 21, No. 4, 441–456, 2007.
42. Joardar, S., "Design development and applications of non redundant instruments for efficient observations in low frequency radio astronomy," Ph.D. Thesis, Univ. Kalyani, 2008.
43. Bhattacharya, A. B., et al., *Astronomy and Astrophysics*, Infinty Science Press, Hingham, 2008 (also Overseas Press India).
44. Fridman, P. A. and W. A. Baan, "RFI mitigation methods in radio astronomy," *J. Astro. & Astroph.*, Vol. 378, 327–344, 2001.

45. Krger, A., *Introduction to Solar Radio Astronomy and Radio Physics*, D. Reidel Pub. Company, Dordrecht, Holland, 1979.
46. Burke, B. F. and F. Graham-Smith, *Introduction to Radio Astronomy*, 2nd edition, Cambridge Univ. Press, UK, 2002.
47. Wu, J., H. Liu, C. Wang, W. Sun, S. Wang, and S. T. Wu, "Applications of synthetic aperture radiometer technology in solar wind remote sensing," *PIERS Online*, Vol. 1, No. 5, 515–519, 2005.
48. Zhang, C., J. Wu, H. Liu, and W. Y. Sun, "Near field imaging of synthetic aperture radiometer," *PIERS Online*, Vol. 4, No. 8, 886–890, 2008.
49. Chan, Y. K. and S. Y. Lim, "Synthetic aperture radar (SAR) signal generation," *Progress In Electromagnetics Research B*, Vol. 1, 269–290, 2008.
50. Chan, Y. K. and V. C. Koo, "An Introduction to synthetic aperture radar (SAR)," *Progress In Electromagnetics Research B*, Vol. 2, 27–60, 2008.
51. Hubert, M. J. C., "Non stationary bistatic synthetic aperture radar processing: Assessment of frequency domain processing from simulated and real signals," *PIERS Online*, Vol. 5, No. 2, 196–200, 2009.
52. Kidera, S., T. Sakamoto, and T. Sato, "Experimental study of shadow region imaging algorithm with multiple scattered waves for UWB radars," *PIERS Online*, Vol. 5, No. 4, 393–396, 2009.
53. Mironov, V. L., P. P. Bobrov, A. S. Yashchenko, I. V. Savin, and A. V. Repin, "Effect of antireflective surface at the radiobrightness observations for the topsoil covered with coniferous litter," *PIERS Online*, Vol. 5, No. 8, 751–755, 2009.